

Coupled amorphous NiFeP/crystalline Ni₃S₂ nanosheets enables accelerated reaction kinetics for high current density seawater electrolysis

Yanyan Song^{a,b}, Xiaoyan Zhang^{a,*}, Zhengyi Xiao^a, Yue Wang^a, Peng Yi^a, Minghua Huang^{b,*}, Lixue Zhang^{a,c,**}

^a College of Chemistry and Chemical Engineering, Collaborative Innovation Center for Hydrogen Energy Key Materials and Technologies of Shandong Province, Qingdao University, Qingdao 266071, China

^b School of Materials Science and Engineering, Ocean University of China, Qingdao 266100, China

^c School of Petroleum and Chemical Engineering, Dongying Vocational Institute, Dongying 257091, China

ARTICLE INFO

Keywords:

Hydrogen
Seawater electrolysis
Amorphous/crystalline interface
Reaction kinetic
Corrosion resistance

ABSTRACT

Rational designing efficient, low-cost and corrosion resistant electrocatalysts is a crucial priority for seawater electrolysis to give impetus to the development of hydrogen energy and carbon neutrality. Herein, an amorphous NiFeP/crystalline Ni₃S₂ (NiFeP/Ni₃S₂) heterojunction catalyst is legitimately constructed for seawater electrolysis. Such structure improves the conductivity of amorphous NiFeP and optimizes the electronic structure by keeping the metal active sites in a relatively high valence state. In situ/ex situ experimental and theoretical calculation results reveal that the amorphous/crystal heterostructure accelerates the reconstruction and reaction kinetics of catalysts, reducing the energy barrier for potential-determining step and leading to improved intrinsic activity. The constructed NiFeP/Ni₃S₂ shows the overpotential of 354 mV to drive current density of 800 mA cm⁻² in the alkaline medium. Besides, under 100 mA cm⁻², NiFeP/Ni₃S₂ can run stably for 600 hours in seawater electrolyte without any hypochlorite production, demonstrating its excellent chemical stability and corrosion resistance.

1. Introduction

Hydrogen is a kind of renewable pollution-free energy carrier, which can integrate intermittent energy (e.g., solar, wind, and tide) to mitigate the overreliance of traditional fossil fuel [1–3]. Numerous researchers have attempted to produce hydrogen by electrochemical water splitting, which contains hydrogen evolution reaction (HER) at cathode and oxygen evolution reaction (OER) at anode [4–6]. However, current water electrolysis technology employs high-purity water as feedstock with commercial-scale hydrogen production, which would lead to a shortage of fresh water resources, especially in arid areas [7,8]. Seawater, accounting for 96.5% of global water reserves, is an ideal electrolyte substitute. Alternative seawater electrolysis is a tempting technology that can be used for hydrogen production and indirect seawater desalination, which has been vigorously developed in the past decade [9,10]. Nevertheless, the practical application of seawater splitting still faces the following hurdles [11–13]. The first obstacle is the unsatisfactory

chlorine evolution reaction (CIER), which competes with OER and generates chlorine species [14]. Under alkaline conditions, OER is dominant within an overpotential of 490 mV [15], providing a convenient potential window to avoid the side CIER. In addition, the notorious chloride ions and other interfering substances in seawater cause unfavorable corrosion to the electrode, shortening the service life of the electrocatalyst [16,17]. Therefore, the excavation of OER catalysts with excellent OER activity, high OER selectivity, and chlorine-corrosion resistance is crucial for seawater splitting.

Amorphous materials have exhibited great potential in the field of electrocatalysis due to its unique physical and chemical properties [18]. The internal atomic arrangement of amorphous materials is long-range aperiodic and short-range ordered, generating ample defects and exposing more active sites [19,20]. Besides, amorphous materials are isotropic and flexible, providing multiple pathways for ion migration [21,22]. In particular, since the abundant unsaturated dangling bonds are more easier to form new chemical bonds to self-heal during

* Corresponding authors.

** Corresponding author at: College of Chemistry and Chemical Engineering, Collaborative Innovation Center for Hydrogen Energy Key Materials and Technologies of Shandong Province, Qingdao University, Qingdao 266071, China.

E-mail addresses: xyzhang@qdu.edu.cn (X. Zhang), huangminghua@ouc.edu.cn (M. Huang), zhanglx@qdu.edu.cn (L. Zhang).

<https://doi.org/10.1016/j.apcatb.2024.124028>

Received 19 February 2024; Received in revised form 26 March 2024; Accepted 1 April 2024

Available online 2 April 2024

0926-3373/© 2024 Elsevier B.V. All rights reserved.

electrocatalytic reconstruction process, amorphous electrocatalysts possess superior corrosion resistance compared to crystalline ones, providing a new opportunity for seawater electrolysis [23]. However, the binding energies of oxygen intermediates with amorphous materials during OER are usually not optimal and the conductivity of the amorphous materials is relatively limited, which restrict their widespread utilizations in seawater splitting [19]. Introducing crystalline phase is a suitable but rare tactic to mend the above drawbacks of the amorphous materials especially for seawater splitting.

Herein, an amorphous NiFeP/crystalline Ni₃S₂ (NiFeP/Ni₃S₂) heterojunction framework was proposed for highly efficient seawater electrolysis by a facile hydrothermal-electrodeposition fabrication. The construction of this heterogeneous interface is not only beneficial for increasing the conductivity of amorphous NiFeP, but also optimizing the Ni d-orbital electronic structure of NiFeP. In situ spectroscopic experiments and *operando* EIS analysis indicate that the amorphous/crystal interface accelerates reaction kinetics and facilitates the generation of relatively high-valent metal active sites during OER process. Density functional theory (DFT) calculations demonstrate that the splendid OER performance is mainly derived from the optimized binding energies of oxygen intermediates to reduce the energy barrier of potential-determining step. The as-obtained NiFeP/Ni₃S₂ exhibits fairly low overpotentials of 256, 329, and 358 mV to reach the current densities of 10, 500, and 1000 mA cm⁻², respectively. Profiting from the splendid corrosion resistance of amorphous NiFeP, the electrolyzer coupled with a NiFeP/Ni₃S₂ anode and a Mo_{0.84}Ni_{0.16} cathode runs stably for more than 600 hours under 100 mA cm⁻² for overall seawater electrolysis, showing great potential for practical AEM water electrolysis. This work depicts a direction for the exploitation of active and robust seawater electrocatalysts through amorphous/crystalline interfaces engineering.

2. Experimental section

2.1. Synthesis of Ni₃S₂

Ni₃S₂ was prepared by a simple hydrothermal reaction. Typically, a piece of NF (3 cm×4 cm) was treated with 3 M HCl, ethanol and deionized water by sonication sequentially for 30 min. The cleaned Ni foam was submerged into a 100 mL Teflon-lined stainless autoclave containing 60 mL of 1.445 mM thiourea solution. The autoclave was sealed and maintained at 160 °C for 5 h. The resulting material was washed with ethanol three times and dried in vacuum at 60 °C, obtaining the Ni₃S₂ material.

2.2. Synthesis of NiFeP/Ni₃S₂

A three-electrode cell with Ni₃S₂ as the working electrode, platinum foil as the counter electrode and Ag/AgCl as the reference electrode was used for NiFeP/Ni₃S₂ fabrication. The precursor electrolyte was prepared by dissolving 0.0038 M Ni(NO₃)₂·6 H₂O, 0.00125 M Fe(NO₃)₃·9 H₂O, 0.5 M NaH₂PO₂ and 0.1 M C₂H₃O₂Na in ultrapure water. The electrodeposition of NiFeP by cyclic voltammetry (CV) was carried out between -1 V and -0.3 V (vs. Ag/AgCl) with a scanning rate of 5 mV s⁻¹ for 10 cycles. After electrodeposition, the NiFeP/Ni₃S₂ (10 C NiFeP/Ni₃S₂) was gently rinsed with ultrapure water and then dried in a vacuum oven. The contrast sample with different electrodeposition cycles were named as 5 C NiFeP/Ni₃S₂, 15 C NiFeP/Ni₃S₂ and 20 C NiFeP/Ni₃S₂, respectively. As presented in Fig. S1, with ten electrodeposition cycles, the as-obtained NiFeP/Ni₃S₂ shows the best OER activity, which was taken as the target electrocatalyst in this work.

2.3. Physical characterizations

The morphologies of the obtained materials were observed by scanning electron microscopy (SEM, Zeiss sigma500, X-MAX50) and transmission electron microscopy (TEM, Tecnai G2F30). The crystalline

structures of the samples were identified by powder X-ray diffraction (XRD, Rigaku D-MAX 2500/PC) using Cu K α radiation. The X-ray photoelectron spectroscopy (XPS) analysis was conducted on an ESCA-LAB 250Xi X-ray photoelectron spectrometer (Thermo Scientific, USA) using Mg K α radiation. The Electron spin resonance (ESR) spectroscopy is tested using Bruker EMXplus-6/1 spectrograph.

2.4. Electrochemical measurements

Electrochemical characterizations of all samples were tested on a Bio-Logic VSP-300 electrochemical workstation. The catalytic activity was determined using a three-electrode configuration, and a carbon rod and Hg/HgO electrode were used as the counter electrode and the reference electrode, respectively. The synthesized samples were used as the working electrodes for OER testing. OER polarization curves with backward scans were collected and plotted with iR compensation (85%) unless otherwise indicated. The catalytic activity was evaluated in different electrolytes (i.e., 1.0 M KOH, 1.0 M KOH + 0.5 M NaCl, 1.0 M KOH + seawater). The natural seawater was collected from the coast of Yellow Sea at Xiaomai Island, Qingdao, China. The collected natural seawater was first filtered by a 0.22 μ m filter membrane to get rid of the pollutants. After adding KOH, the sample was centrifuged to remove the precipitate and used as the electrolyte. All the measured potentials vs. Hg/HgO were converted to the reversible hydrogen electrode (RHE) by the equation: $E_{RHE} = E_{Hg/HgO} + 0.098 V + 0.059 pH$. The electrochemical active surface area (ECSA) was tested in the non-Faraday region. The electrochemical impedance spectra (EIS) were measured from 0.1 Hz to 100 KHz at 1.374 V vs. RHE for OER. The TOF values are calculated through the following equation: $TOF = |j|A/(mFn)$, where $|j|$ is the delivered current density at a potential during the LSV test. A represents the electrode area and F is the Faradaic constant (96485 C mol⁻¹). n represents the electron transfer numbers in OER.

2.5. In situ Raman measurements

The Raman spectra were collected with an inverted Raman spectroscopy system, which combines a PI spectrometer (PIX2560-SF-Q), 532 nm laser (MSL-III-532 nm-100Mw-19021075) and Olympus inverted microscope (IX73). Measurements were performed on an Au electrode that was loaded with catalyst powder as the working electrode using a homemade electrochemical cell setup. A Pt wire was used as the counter electrode and an Ag/AgCl electrode as the reference electrode in a 1.0 M KOH electrolyte.

2.6. Computational methods

To compare the geometric and electronic structures, and the OER activity of Ni₃S₂, NiFeP, and NiFeP/Ni₃S₂ compound, the density functional theory (DFT) calculations were carried out using the Vienna ab-initio simulation package (VASP). To describe the electron ion interaction and exchange correlation energy, the projected augmented wave (PAW) potential and generalized gradient approximation (GGA) of the spin-polarized Perdew-Burke-Ernzerhof (PBE) functional were employed, respectively. The energy cutoff for the plane-wave expansion was set as 400 eV for optimizing calculations of atoms and cell optimization. The first Brillouin zone was sampled in the Monkhorst-Pack grid. The 3×3×1 k-point mesh was applied for the surface calculation. The electronic structures of the catalysts were calculated by the density of state (DOS) with much dense 5×5×1 k-point mesh, while the other calculation parameters were same with the geometric optimization. To describe the van der Waals interactions between the adsorbed intermediates and catalysts, the DFT-D3 method was adopted. The construction of studied models was based on the crystal structures of Ni₃S₂ and NiFeP. The (001) surface with 2 × 2 × 1 supercell and three layers was cut from the bulk Ni₃S₂. To build the amorphous NiFeP model, one NiFeP cluster with 28 atoms was run from 300 K to 2000 K for a period of

10 ps with a time step of 1.0 fs in the AIMD simulations. To build the model of NiFeP/Ni₃S₂ compound, the amorphous NiFeP cluster was placed on the Ni₃S₂ (001) surface for the structural optimization calculations. The most bottom atoms were fixed and the other atoms were allowed to relax. To avoid the periodic interactions, the vacuum spacing along the c direction perpendicular to the catalyst surface was as large as 15 Å. For geometry optimization, the energy converged to 1.0×10^{-5} eV/atom and the force converged to 0.01 eV/Å were set as the convergence criterion. The Gibbs free-energy change of adsorbed intermediates (ΔG_{ads}) on the catalysts was used to evaluate the OER activities of different catalysts, which was defined as follows: $\Delta G_{ads} = \Delta E_{ads} + \Delta E_{ZPE} - T\Delta S$, where ΔE_{ads} is the adsorption energy of intermediates on the catalysts. ΔE_{ZPE} is the zero-point energy correction, $T\Delta S$ is the entropy correction at the temperature of T before and after the adsorption.

3. Results and discussion

3.1. Synthesis and characterization

The NiFeP/Ni₃S₂ nanoarray was fabricated through the sequential hydrothermal and electrochemical deposition procedures, as diagrammatically described in Scheme S1 (Supporting information). Ni₃S₂ was grown on nickel foam (NF) through the hydrothermal reaction using NF and thiourea as nickel and sulfur sources, respectively. In the XRD pattern of Ni₃S₂ in Fig. S2, the peaks at 31.1°, 37.8°, 50.1° and 55.2° can be indexed to (110), (003), (211) and (122) planes of hexagonal Ni₃S₂ phase (JCPDS No. 97-065-7413). SEM images in Fig. 1a and Fig. S3 show that the Ni₃S₂ nanosheets are uniformly distributed on NF and interleaved with each other. The crystal structure of Ni₃S₂ was further identified by the high-resolution transmission electron microscopy (HRTEM) and selected area electron diffraction (SAED). As described in Fig. 1b, the evident lattice fringe of 0.286 nm is assigned to (110) plane of Ni₃S₂, which is consistent with the SAED pattern with ordered arrays

of diffraction spots (Fig. 1c), indicating the well-defined crystallinity of Ni₃S₂ nanosheets.

NiFeP was then directly electrodeposited onto the Ni₃S₂ surface to construct NiFeP/Ni₃S₂ amorphous/crystalline heterostructure [24]. Compared with that of Ni₃S₂, as illustrated in Fig. S2, no additional diffraction peaks were observed in the XRD pattern of NiFeP/Ni₃S₂, reflecting the possible amorphous structure formed by electrodeposition. The SEM image in Fig. 1d discloses that the electrodeposition of NiFeP did not give rise to the change of the Ni₃S₂ nanosheet skeleton, but the thickness of the nanosheet is obviously increased from ~52 nm to ~68 nm. In HRTEM image (Fig. 1e), the heterointerface between the crystalline Ni₃S₂ and the amorphous NiFeP outer layer (marked by the yellow and red dashed lines) is clearly observed. The bright spots related to Ni₃S₂ and diffusive diffraction rings representing amorphous NiFeP in SAED pattern (Fig. 1f) are also in accordance with the above XRD and TEM analysis. The high-angle annular dark-field scanning transmission electron microscopy (HAADF-STEM) coupled with energy-dispersive X-ray spectroscopy (EDX) elemental mappings in Fig. 1g illustrate the coexist and uniform distribution of Ni, S, Fe, and P elements on the entire nanosheet. In brief, the above results confirm that the NiFeP/Ni₃S₂ amorphous/crystalline heterointerfaces were successfully created.

X-ray photoelectron spectroscopy (XPS) technique was applied to probe the chemical composition and valence state of NiFeP/Ni₃S₂. As presented in Fig. 2a, the peaks of Ni, Fe, S, and P can be obviously identified in the survey spectra of NiFeP/Ni₃S₂, which is in agreement with TEM-EDS result. The peaks situated at 497.8 eV in the XPS survey spectra of NiFeP/Ni₃S₂ and NiFeP are recognized as Na Auger signal [25, 26], which is derived from the utilization of C₂H₃O₂Na and NaH₂PO₂ during the electrodeposition of amorphous NiFeP. For the high-resolution Ni 2p_{3/2} spectra (Fig. 2b), the strong peaks at 855.4 eV and 856.5 eV are corresponding to Ni²⁺ and Ni³⁺ species, respectively. The signal situated at 852.3 eV is allocated to Ni-P bond. Obviously, a positive shift for Ni³⁺ peak can be judged in NiFeP/Ni₃S₂, indicating a

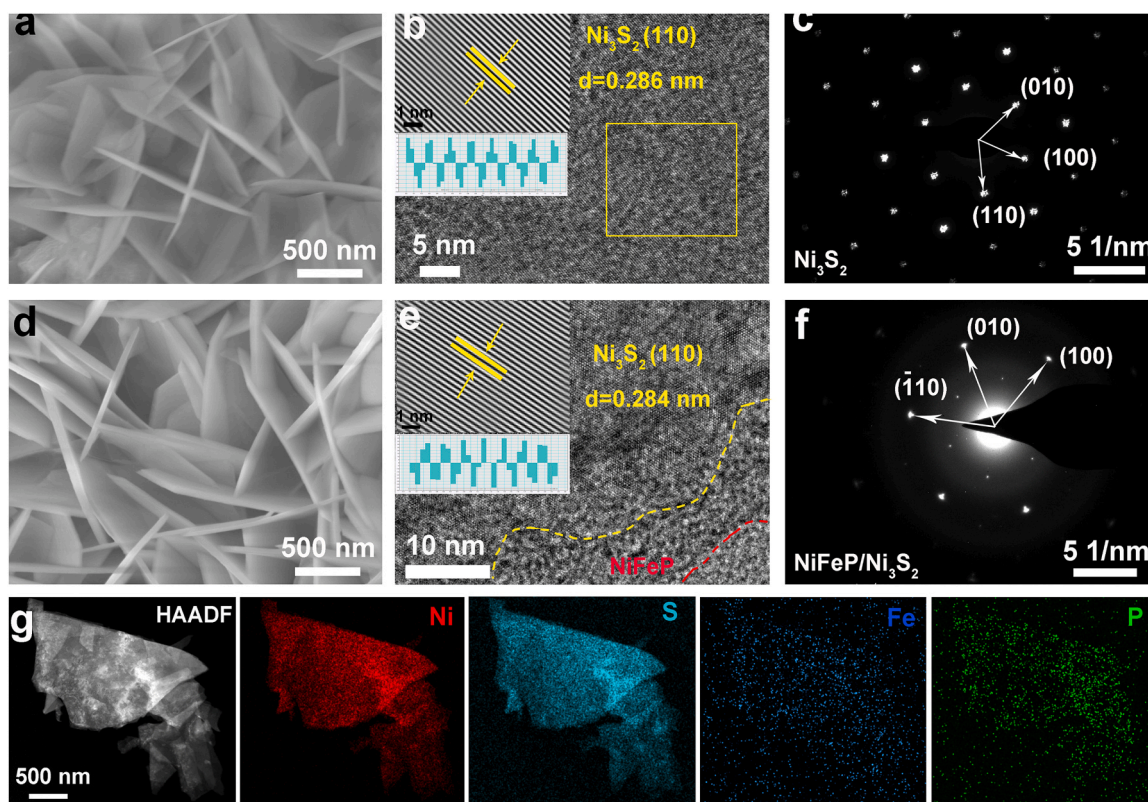


Fig. 1. (a) SEM image, (b) HRTEM image, and (c) SAED pattern for Ni₃S₂. (d) SEM image, (e) HRTEM image, (f) SAED pattern, and (g) EDX element mapping for NiFeP/Ni₃S₂.

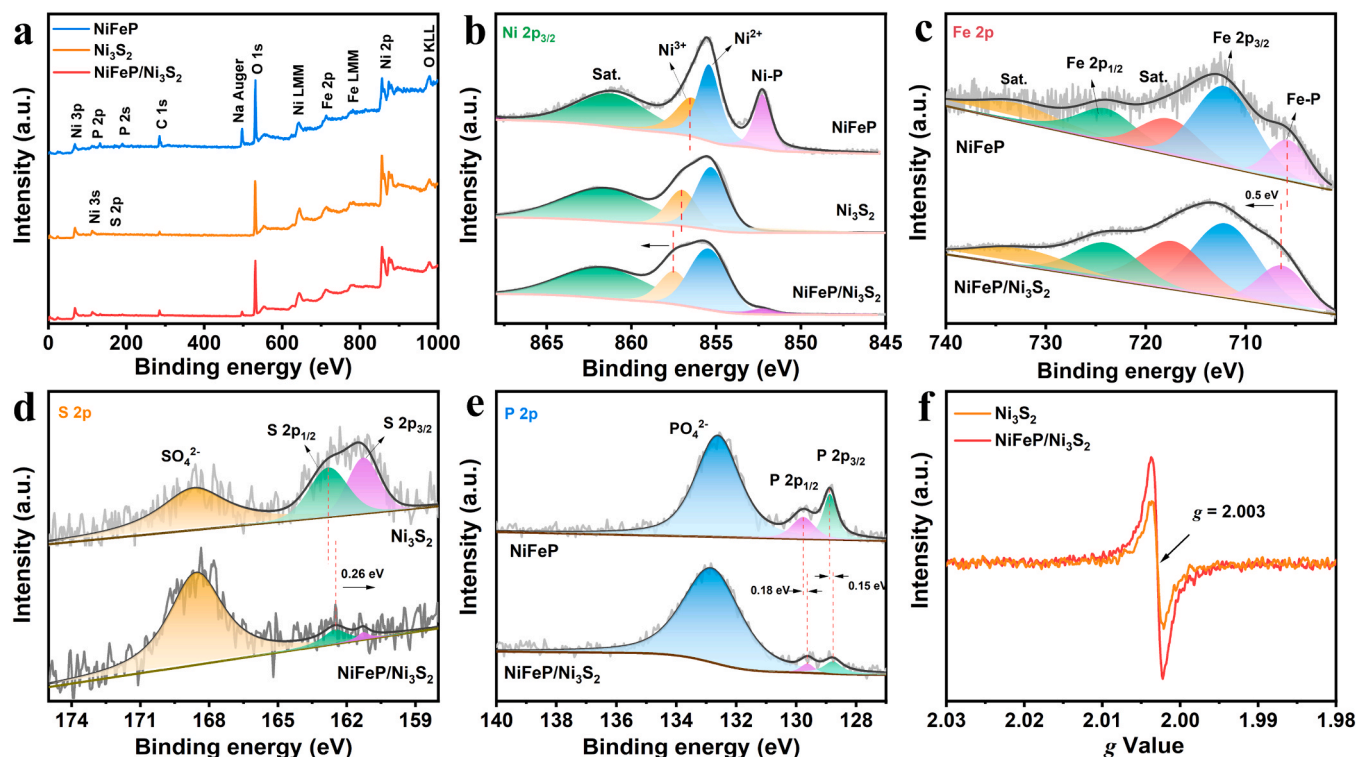


Fig. 2. (a) XPS survey spectra. High-resolution (b) Ni 2p, (c) Fe 2p, (d) S 2p, (e) P 2p XPS spectra of NiFeP, Ni₃S₂, and NiFeP/Ni₃S₂. (f) Room-temperature ESR spectra of Ni₃S₂ and NiFeP/Ni₃S₂.

higher oxidation state of Ni after the formation of the interface [27–29]. In the Fe 2p spectra (Fig. 2c), a pair of peaks with binding energies of 712.0 eV and 723.8 eV, accompanied by corresponding satellite peaks, are attributable to Fe 2p_{3/2} and Fe 2p_{1/2}, respectively. The Fe-P bond in NiFeP/Ni₃S₂ (706.3 eV) has a positive shift than that in NiFeP (705.8 eV) [30,31]. The peak fitting of the S 2p spectra (Fig. 2d) displays the pair peaks (~161.3 eV and ~162.7 eV) and the broad peak (~168.6 eV), which can be ascribed to the S-metal bond and superficial S-O bond, respectively [32]. The S-metal peak intensity in NiFeP/Ni₃S₂ was weakened compared with that in Ni₃S₂, which is possibly due to the S element being located in the inner layer. In the high-resolution P 2p spectra (Fig. 2e), the binding energies of 128.8 eV and 129.6 eV can be assigned to P 2p_{3/2} and P 2p_{1/2}, respectively, while the binding energy of 132.8 eV can be indexed to P-O bond [33]. The apparent shifts of Ni 2p, Fe 2p, S 2p and P 2p peak positions among NiFeP/Ni₃S₂ indicate the strong electron interaction after amorphous/crystalline interface coupling, and the overall electron transfer trend is from NiFeP to Ni₃S₂ owing to the much more electronegativity of S (2.58) than that of P (2.19) [34,35]. ESR spectroscopy was performed to evaluate the defect degree by trapping the unpaired electrons in the nanomaterials. In Fig. 2f, both Ni₃S₂ and NiFeP/Ni₃S₂ exhibit ESR signals at $g = 2.003$, which could be identified as the electrons trapping. The ESR intensity of NiFeP/Ni₃S₂ is stronger than that of Ni₃S₂, indicating the higher defect concentration in the built NiFeP/Ni₃S₂ structure, which would regulate the electronic structure of metal sites and optimize the adsorption of oxygen-containing intermediates to establish favorable conditions for rapid reconstruction during OER process [36].

3.2. Evaluation of electrocatalytic OER performance

The OER activities of all electrocatalysts were firstly evaluated by linear sweep voltammetry (LSV) technique in the three-electrode setup in 1.0 M KOH. As shown in Fig. 3a and Fig. S4, the NiFeP/Ni₃S₂ heterogeneous electrocatalyst only requires the overpotentials of 256, 301 and 329 mV to drive current densities of 10, 100 and 500 mA cm⁻²,

respectively, which is dramatically smaller than those of NiFeP and Ni₃S₂, confirming the effectiveness of establishing the amorphous/crystalline heterojunction in increasing the OER activity. Meanwhile, the OER performance of NiFeP/Ni₃S₂ is also superior to that of the classical OER benchmark catalyst RuO₂ [37]. The kinetic parameter, Tafel slope (Fig. 3b) obtained from the LSV, demonstrates that NiFeP/Ni₃S₂ has a smaller value of 36.1 mV dec⁻¹ than NiFeP (63.0 mV dec⁻¹), Ni₃S₂ (100.8 mV dec⁻¹) and RuO₂ (52.0 mV dec⁻¹), further verifying the excellent OER kinetics of NiFeP/Ni₃S₂ in alkaline electrolytes. Moreover, the electrochemical impedance spectroscopy (EIS) (Fig. 3c and Table S1) data reveal that NiFeP/Ni₃S₂ possesses the lowest charge transfer resistance (R_{ct}), demonstrating the outstanding charge transfer rate by constructing the amorphous/crystalline heterostructure. Additionally, integrating the calculated electrochemically double-layer capacitance (C_{dl}) values determined from CV curves at the non-Faradaic region with different scan rates (Fig. S5) displays that NiFeP/Ni₃S₂ exposes higher electrochemically active surface area (ECSA) relative to other samples (Fig. 3d), indicating the reasonable combination of NiFeP and Ni₃S₂ provides more surface-active sites [38]. In the ECSA-normalized LSV curves, NiFeP/Ni₃S₂ catalyst still exhibits smaller overpotential compared to NiFeP and Ni₃S₂, suggesting its excellent intrinsic OER catalytic activity (Fig. 3e). The improvement of the intrinsic OER performance of NiFeP/Ni₃S₂ was further investigated by the turnover frequencies (TOFs) based on the CV charge capacity (Fig. S6). It is noteworthy that the NiFeP/Ni₃S₂ shows a much higher TOF value (0.497 s⁻¹) at the overpotential of 350 mV than those of NiFeP and Ni₃S₂ (Fig. 3f), revealing again its higher intrinsic catalytic activity toward OER.

To verify the practicability of the catalyst, the OER activity of NiFeP/Ni₃S₂ was further conducted in alkaline simulated seawater (1.0 M KOH + 0.5 M NaCl) and alkaline natural seawater (1.0 M KOH + seawater). As shown in Fig. 3g, NiFeP/Ni₃S₂ well retains the catalytic activity 1.0 M KOH + 0.5 M NaCl, requiring the overpotentials of 266 mV and 348 mV to reach current densities of 10 and 500 mA cm⁻², respectively. In 1.0 M KOH + seawater, by contrast, NiFeP/Ni₃S₂ demands overpotentials of

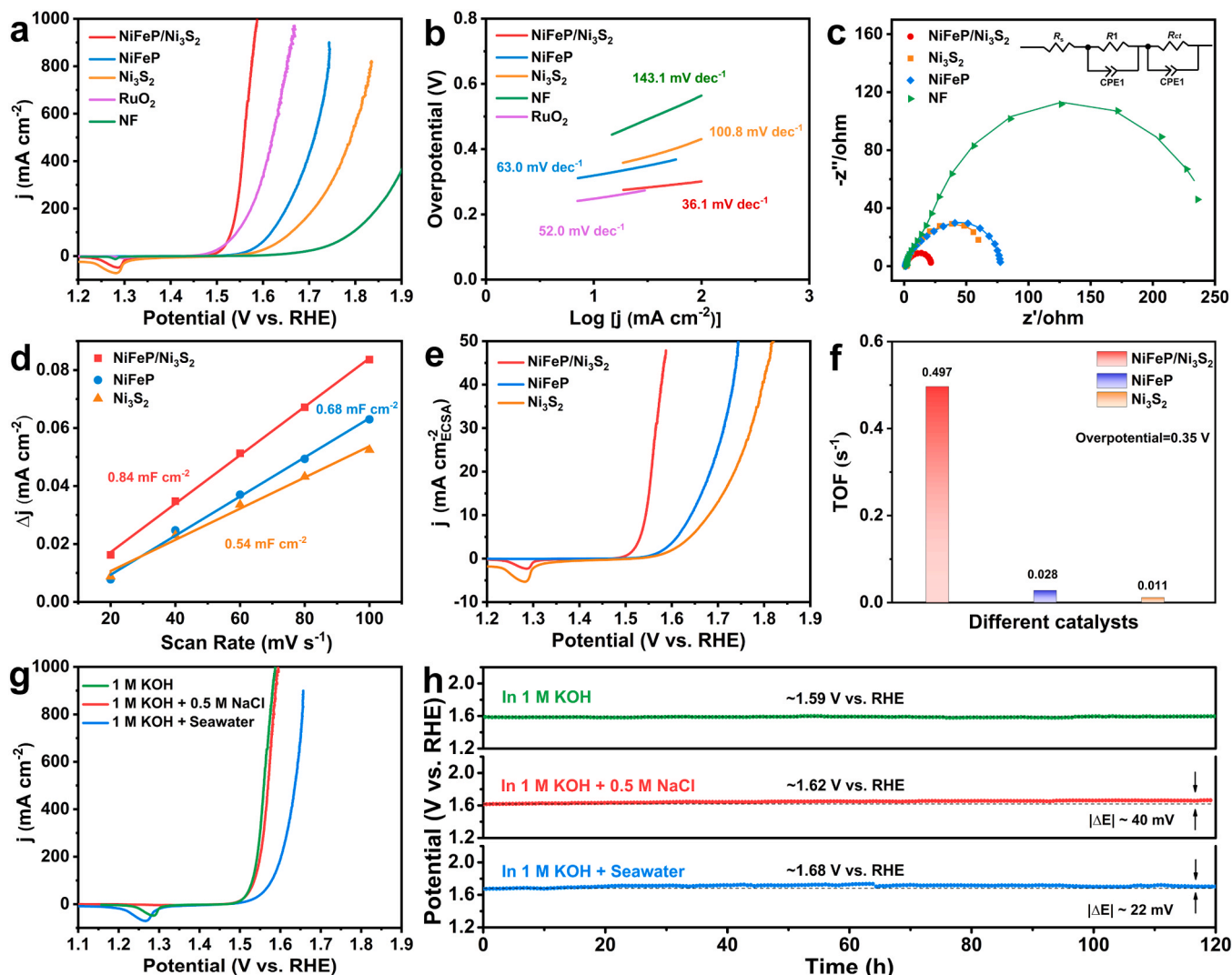


Fig. 3. (a) LSV curves, and (b) the corresponding Tafel plots of NiFeP/Ni₃S₂ and other catalysts in 1.0 M KOH. (c) EIS Nyquist plots and the equivalent circuit diagram, (d) capacitive currents at -0.37 V (vs. Hg/HgO) as a function of the scan rate, (e) the ECSA-normalized LSV curves, and (f) TOF values for Ni₃S₂, NiFeP, and NiFeP/Ni₃S₂. (g) Polarization curves for the NiFeP/Ni₃S₂ electrode tested in different electrolytes. (h) Long-term stability tests at a constant current density of 100 mA cm⁻² for the NiFeP/Ni₃S₂ electrode in 1.0 M KOH, 1.0 M KOH + 0.5 M NaCl and 1.0 M KOH + seawater, respectively.

282 mV and 406 mV to achieve current densities of 10 and 500 mA cm⁻², respectively. Such activity attenuation may be derived from electrode poisoning by natural seawater pollutants such as bacteria, microorganisms, and small particles. Even in this harsh environment, the catalyst needs only an overpotential of 424 mV to reach an industrial-scale current density of 800 mA cm⁻², which is still far below the triggering overpotential (490 mV) of CLER. Compared with the recently reported other catalysts, NiFeP/Ni₃S₂ exhibited comparable and even better performance towards seawater electrolysis (Table S2).

Stability is another critical indicator to be reckoned with for the electrocatalyst especially from the perspective of industrial applications. Therefore, a series of chronoamperometric measurements were carried out. As displayed in Fig. 3h, negligible fluctuation of the applied potential can be observed when testing the durability of NiFeP/Ni₃S₂ at the current density of 100 mA cm⁻² in 1.0 M KOH, 1.0 M KOH + 0.5 M NaCl and 1.0 M KOH + seawater. The structural stability of NiFeP/Ni₃S₂ after operation in alkaline seawater was also characterized (Fig. S7). The nanosheet array skeleton of NiFeP/Ni₃S₂ is well maintained and the surface of the nanosheet becomes rough after prolonged durability test, which may be caused by the surface reconstruction of the catalyst and the generation of oxygen bubbles during the OER process. The Ni₃S₂ phase and the amorphous/crystal heterogeneous interface were also

well preserved from the HRTEM characterization. XPS was then proceeded to analyze the element valence state changes of the NiFeP/Ni₃S₂ after OER stability test for 120 hours. As described in Fig. S8a, the high-resolution XPS spectra of Ni 2p_{3/2} in NiFeP/Ni₃S₂ indicate that the peak relevant to the Ni-P bond significantly is decreased and the ratio of Ni²⁺/Ni³⁺ is reduced from (2.05) to (0.97), which can be attributed to the formation of active nickel (oxy)hydroxide species. Similarly, the Fe 2p spectra (Fig. S8b) show the increase of the Fe valence state after OER. In the S 2p spectra (Fig. S8c), the peak intensity becomes less pronounced, which may be due to the surface oxidation at high potential. Phosphides are oxidized to PO₄³⁻ species in the P 2p spectra (Fig. S8d), which plays a critical role in repelling Cl⁻ ions and enhancing the corrosion resistance of the catalyst [39]. In brief summary, the above results indicate the excellent structural stability and corrosion resistance of the NiFeP/Ni₃S₂ catalyst.

3.3. Mechanism for the enhanced OER and stability

For understanding the enhanced OER performance of the NiFeP/Ni₃S₂ catalyst, we carried out corrosion polarization tests, operando measurements and DFT calculations. Firstly, the corrosion polarization curves were measured to elucidate the corrosion resistance capability of

the electrodes in natural seawater (Fig. 4a and Table S3) [40]. As expected, the amorphous NiFeP layer exhibits the highest corrosion potential (-0.115 V vs. SCE) and the lowest corrosion current density ($6.49 \times 10^{-7} \text{ A cm}^{-2}$), indicating its fantastic chloride corrosion resistance ability. Compared with that of bare amorphous NiFeP, the corresponding corrosion potential of the heterostructure NiFeP/Ni₃S₂ declines to -0.185 V vs. SCE and the corrosion current density increases to $2.00 \times 10^{-6} \text{ A cm}^{-2}$. However, it is still much better than those of pristine Ni₃S₂ (-0.230 V vs. SCE and $1.35 \times 10^{-5} \text{ A cm}^{-2}$, respectively), signifying that the establishment of NiFeP/Ni₃S₂ heterogeneous interface can not only take advantage of the superb corrosion resistance ability of the amorphous NiFeP but also effectively improve the catalyst activity (Fig. 3a) and stability (Fig. 3h and Fig. S9).

In-situ Raman spectroscopy was then performed to identify real active sites and dynamic transformation. Two characteristic peaks at the wave numbers of 473 cm^{-1} (e_g bending vibration) and 550 cm^{-1} (A_{1g} stretching vibration) can be designated as Ni^{III}-O in γ -NiOOH, which is consistent with the above XPS results [41]. Notably, the applied potential for triggering the appearance of Ni^{III}-O signals in NiFeP/Ni₃S₂ (1.40 V, Fig. 4c) is much lower than that of bare Ni₃S₂ (1.55 V, Fig. 4b), highlighting the faster reconstruction process for NiFeP/Ni₃S₂ amorphous/crystalline catalyst. The relative intensity of I_{473}/I_{550} implies structural defects and disorder of the lattice of active NiOOH. Fitted

peak relative intensity of I_{473}/I_{550} for NiFeP/Ni₃S₂ at 1.60 V are higher than that of Ni₃S₂, declaring that the heterogeneous interface between amorphous NiFeP and crystal Ni₃S₂ can effectively accelerate the reconstruction of catalyst and the formation of active γ -NiOOH species [42].

Furthermore, the *operando* EIS under working conditions was used to track the dynamic reconstruction process of catalysts in 1.0 M KOH (Figs. 4d and e). The peaks of phase angle at high-frequency come from the electron conduction in the inner layer of the catalyst [31]. Below 1.35 V, the high-frequency equivalent resistance (R1) of Ni₃S₂ and NiFeP/Ni₃S₂ were large (Fig. 4f and Table S4), indicating extremely weak charge transfer. When the voltage reaches 1.35 V, a rapidly decreased R1 is observed, which is due to the electrooxidation converting Ni^{II} to Ni^{III}, indicating the rapid reconstruction and the high catalytic activity of NiFeP/Ni₃S₂ [43]. This is conducive to achieving high catalytic activity quickly. At the low-frequency region, the phase angle peak of NiFeP/Ni₃S₂ is lower than that of Ni₃S₂, indicating that the construction of heterojunction surfaces can promote charge transfer at the electrolyte-catalyst interface reaction and thus accelerate OER kinetics [44]. In addition, the fitting impedance representing OER (R2) occurred at low frequency range is decreased with increasing voltage. At the same voltage, the R2 of NiFeP/Ni₃S₂ is smaller than that of Ni₃S₂, verifying its better activity and faster kinetics.

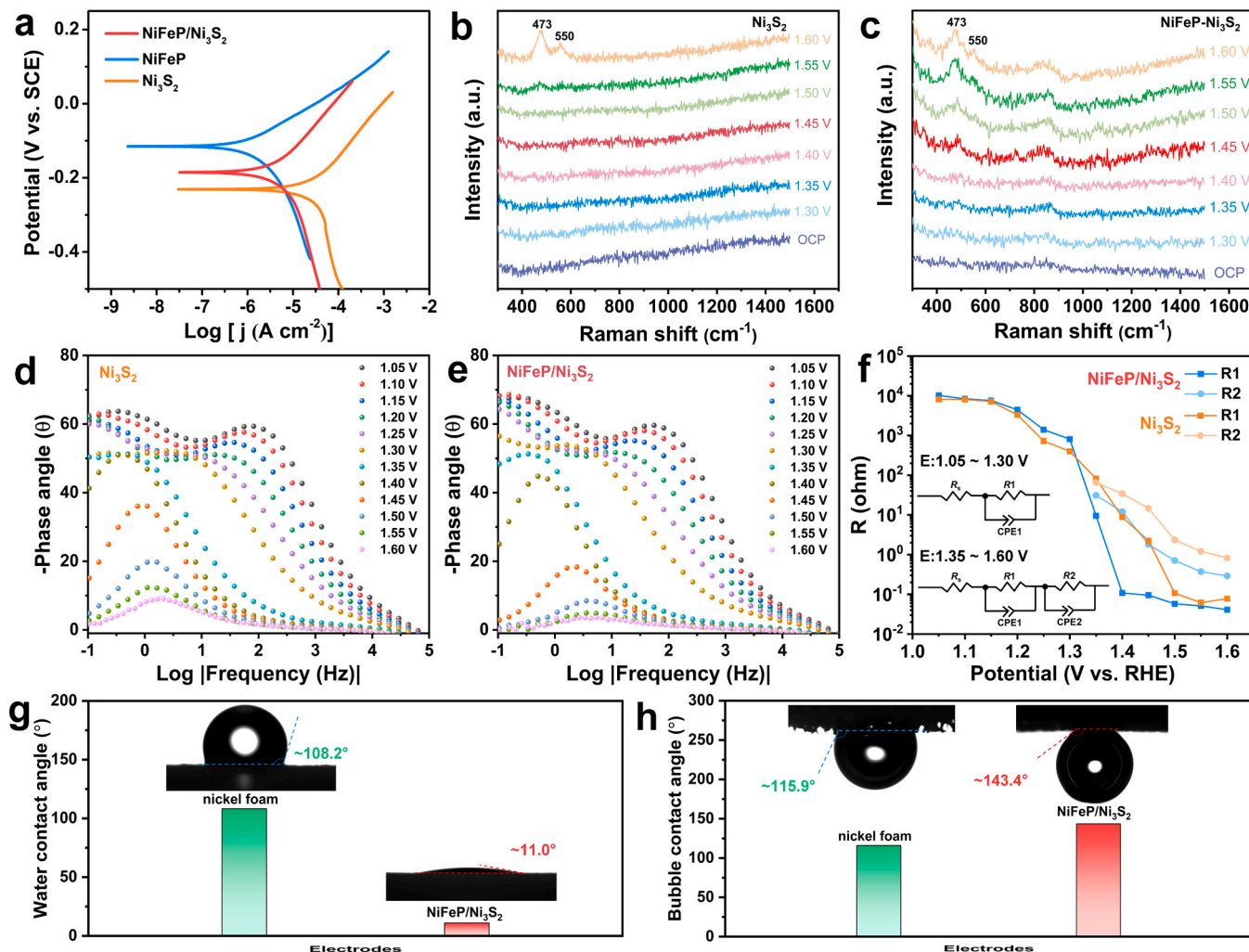


Fig. 4. (a) Corrosion polarization plots of NiFeP/Ni₃S₂, NiFeP and Ni₃S₂ electrodes in natural seawater. In-situ Raman spectra of (b) NiFeP/Ni₃S₂ and (c) Ni₃S₂ at various potentials. Bode plots of (d) Ni₃S₂ and (e) NiFeP/Ni₃S₂ for OER at different potentials in 1.0 M KOH. (f) Correlation of equivalent resistances (R1 and R2) and potentials for Ni₃S₂ and NiFeP/Ni₃S₂. The diagrams embedded are the individual equivalent circuit models. (g) Water contact angles and (h) underwater gas-bubble contact angles of the NiFeP/Ni₃S₂ and bare NF electrodes.

To meticulously prove the ascendancy of the NiFeP/Ni₃S₂ nanoarrays, water and gas contact angles (CAs) were measured. The water CAs of nickel foam (NF) and NiFeP/Ni₃S₂ are about 108.2° and 11.0° (Fig. 4g), respectively, indicating the remarkable electrolyte wettability of NiFeP/Ni₃S₂ to promote mass transfer [45]. Furthermore, the gas CAs for NF and NiFeP/Ni₃S₂ are about 115.9° and 143.4° (Fig. 4h), respectively. Such splendid aerophobicity can not only accelerate the reaction kinetics effectively by improving the utilization frequency of catalytic sites via fast oxygen bubbles desorption but also strengthen the mechanical stability of the electrode [46]. The marvelous wettability and aerophobicity of NiFeP/Ni₃S₂ allow excellent reactant diffusion and product escaping [47], which is essential for electrocatalytic reactions at industrial current density level.

3.4. Theoretical calculation

To elucidate the impact of the amorphous/crystal interface on the electronic structure as well as the OER mechanism, DFT calculations were conducted. Based on the optimized atomic models of NiFeP, Ni₃S₂, and NiFeP/Ni₃S₂ (Fig. 5a and Fig. S10), the differential charge density distribution was firstly investigated. It can be obviously seen from the

Bader charge analysis (Fig. 5b) that 1.38 e is transferred from NiFeP to Ni₃S₂, suggesting that the constructed NiFeP/Ni₃S₂ can enhance the electron transfer and optimize the electronic structure of NiFeP. As previously reported, the charge transfer ability at interface is closely related to the electron escaping difficulty, which can also be reflected by work function (WF) [48]. Hence, the WF values for NiFeP and Ni₃S₂ are calculated (Fig. 5c). The smaller WF value of NiFeP (4.43 eV) compared to that of Ni₃S₂ (5.38 eV) results in higher Fermi level, inducing the interfacial electron transfer from NiFeP to Ni₃S₂ and the construction of a stable built-in electric field to manipulate the higher electronic states of the metal sites for NiFeP (Fig. 5d), which is in accordance with the above XPS data and Bader charge analysis. Density of states (DOS) is used to gain insight into the intrinsic electronic properties and the influence on the adsorption of key intermediates during OER. As depicted in Fig. S11, the electron states around the Fermi Level (E_F) are mainly stem from Ni 3d orbitals, illustrating the active center of the catalyst is Ni site. Moreover, NiFeP/Ni₃S₂ exhibits the highest density of states around E_F (Fig. 5e), indicating the superb electrical conductivity and increased electron mobility in NiFeP/Ni₃S₂. According to the d-band center theory, the electron density near E_F can affect the adsorption of intermediates on catalyst surface. The d-band center of Ni 3d in

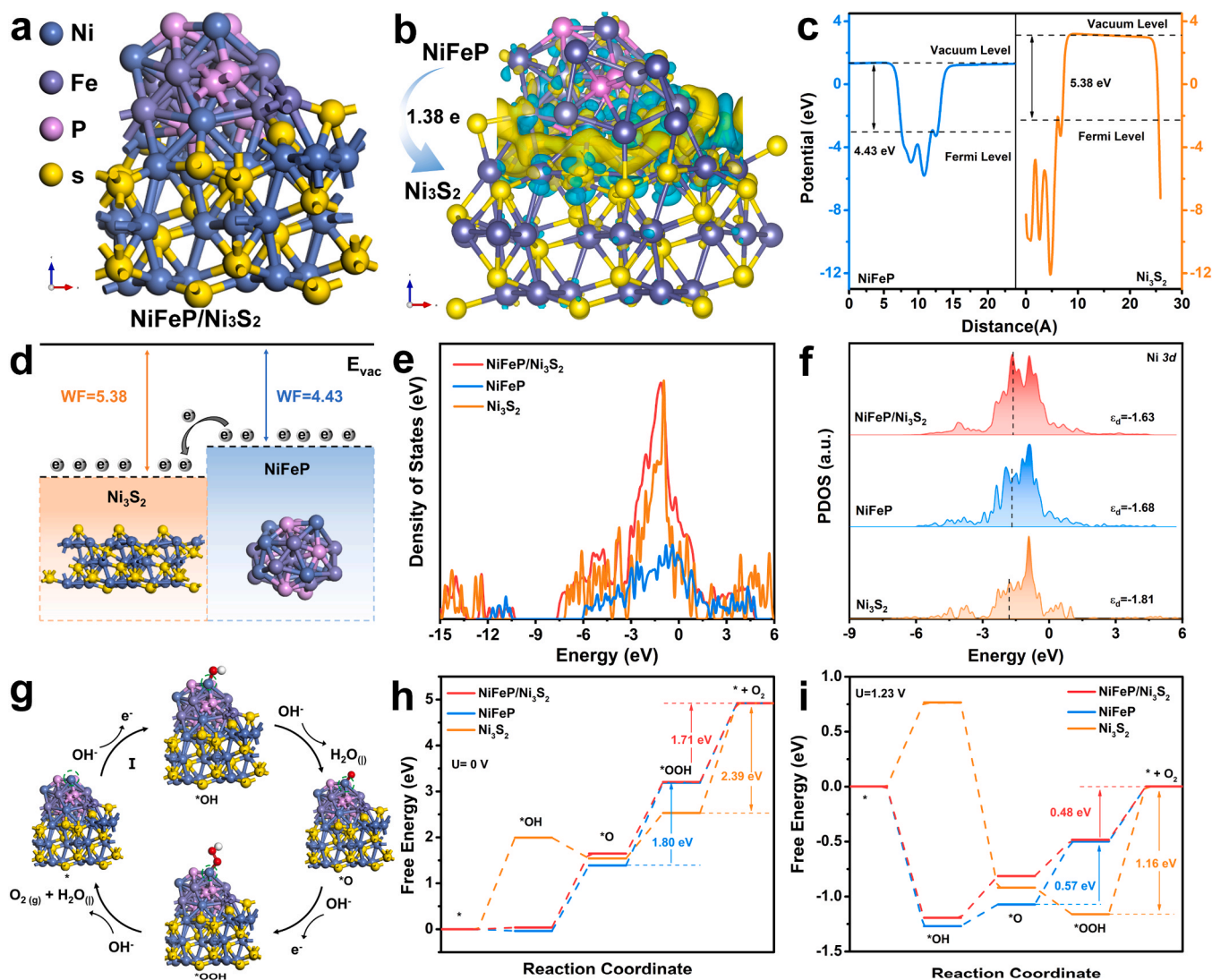


Fig. 5. (a) The optimized atomic model of NiFeP/Ni₃S₂ and (b) the corresponding differential charge density distribution map at the interface. Yellow and cyan indicate electron accumulation and depletion, respectively. (c) Work function values of NiFeP and Ni₃S₂. (d) Charge transfer process in NiFeP/Ni₃S₂. (e) DOS, and (f) PDOS of NiFeP, Ni₃S₂ and NiFeP/Ni₃S₂. (g) The adsorption configuration of key intermediates during OER on NiFeP/Ni₃S₂ catalyst. (h, i) Free energy for the OER pathways on NiFeP, Ni₃S₂ and NiFeP/Ni₃S₂ at $U=0$ V and $U=1.23$ V, respectively.

NiFeP/Ni₃S₂ (-1.63 eV) is much closer to E_F in comparison with those in NiFeP (-1.68 eV) and Ni₃S₂ (-1.81 eV) (Fig. 5f), suggesting much optimized adsorption strength with the oxygen intermediates during OER. Gibbs free energies were further calculated to understand the OER pathway, in which proton-coupled electron transfer is included (Fig. 5g). The OER free energy profiles of the catalysts at $U = 0$ are presented in Fig. 5h, in which all the elementary reactions undergo an uphill (endothermic) process. The potential-determining step (PDS) for both Ni₃S₂ and NiFeP/Ni₃S₂ is the formation of O₂ from *OOH with the energy barriers of 2.39 and 1.71 eV, respectively, while the PDS for NiFeP is the conversion from *O to *OOH with an energy barrier of 1.80 eV. The results show that the NiFeP/Ni₃S₂ heterointerface structure can not only change the PDS but also decrease the free energy barrier of PDS, thus resulting in much better OER activity. At $U = 1.23$ V, the results obtained are consistent with those obtained at $U = 0$.

3.5. Evaluation of electrocatalytic activity for overall seawater splitting

Finally, a two-electrode electrolyzer (Fig. 6a) was assembled by

selecting NiFeP/Ni₃S₂ and the previously reported HER catalyst Mo_{0.84}Ni_{0.16} in our group [49] as the anode and cathode, respectively. The NiFeP/Ni₃S₂||Mo_{0.84}Ni_{0.16} electrolyzer delivers the current density of 100 mA cm⁻² at a small potential of 1.79 V in 1.0 M KOH, which is even lower than that of the benchmark RuO₂||Mo_{0.84}Ni_{0.16} couple (1.94 V). Remarkably, the electrolyzer still retained excellent water splitting activity even in alkaline simulated seawater and natural seawater (Fig. 6b). Additionally, Faradaic efficiency of the two-electrode cell in 1.0 M KOH + seawater was calculated via drainage method by calculating the volume of the collected H₂ and O₂ (Fig. 6c), which is infinitely close to 2:1, and the actual production is consistent with the theoretical value, which entails that the catalyst has a nearly 100% Faradaic efficiency for seawater splitting.

From the viewpoint of industrial application, the operating durability of the electrolyzer is also a non-negligible metric to gauge. In 1.0 M KOH + seawater, the NiFeP/Ni₃S₂||Mo_{0.84}Ni_{0.16} electrolyzer can run stably for more than 600 hours with the degradation of only 72 mV, denoting the superiorities of the NiFeP/Ni₃S₂ catalyst for producing hydrogen from seawater splitting (Fig. 6d). After prolonged electrolysis,

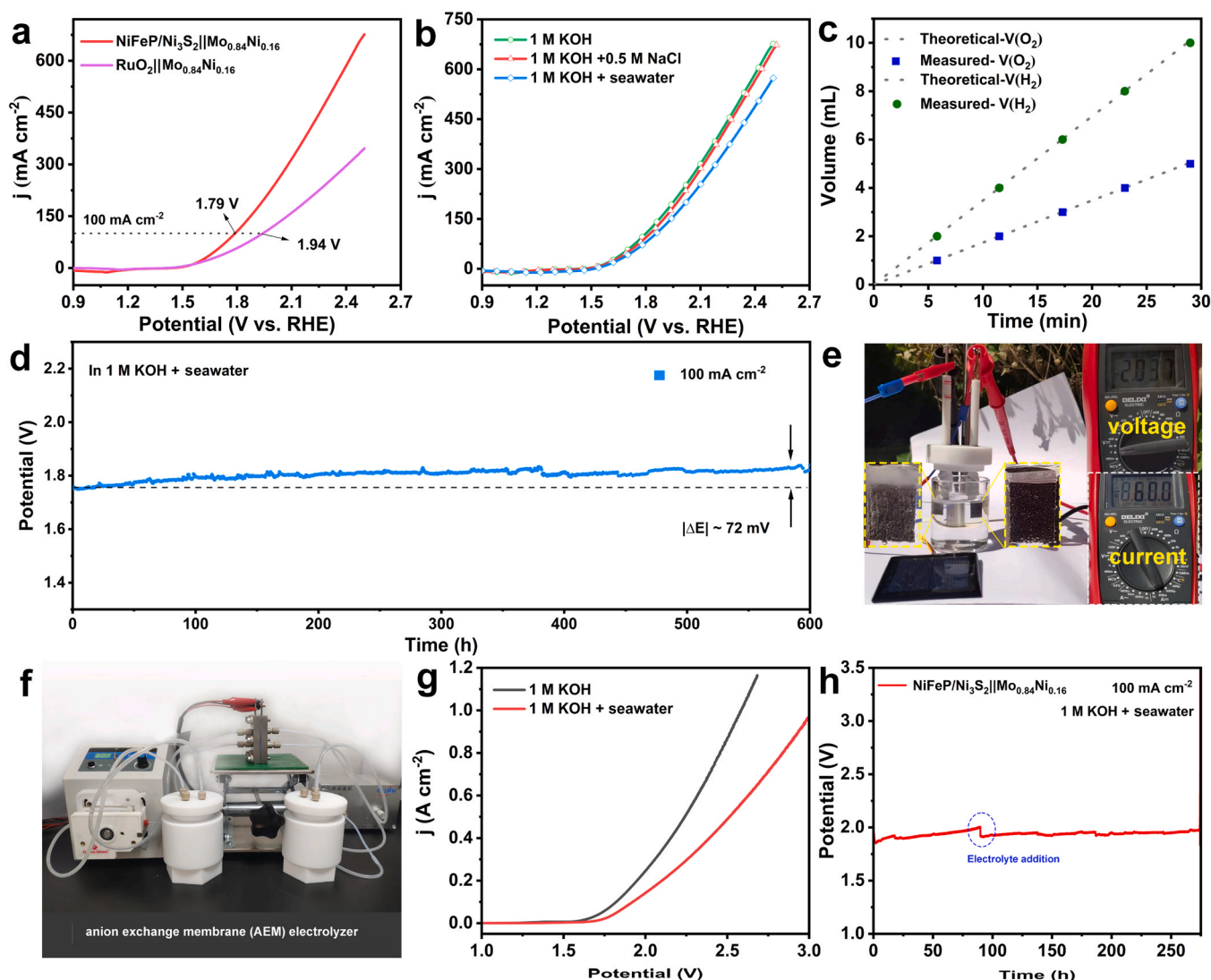


Fig. 6. (a) The polarization plots without iR compensation for NiFeP/Ni₃S₂||Mo_{0.84}Ni_{0.16} and RuO₂||Mo_{0.84}Ni_{0.16} in 1.0 M KOH. (b) The polarization plots of NiFeP/Ni₃S₂||Mo_{0.84}Ni_{0.16} in different electrolytes. (c) Comparison between the amounts of collected and theoretical gaseous products (H₂ and O₂) by the two-electrode electrolyzer at a constant current density of 100 mA cm⁻² in 1.0 M KOH + seawater. (d) Durability test conducted at a constant current density of 100 mA cm⁻² in 1.0 M KOH + seawater. (e) Photograph of the overall water electrolyzer powered by commercial solar cell. (f) Photograph of the AEM electrolyzer. (g) Polarization curves without iR compensation of NiFeP/Ni₃S₂||Mo_{0.84}Ni_{0.16} in 1.0 M KOH + seawater at 25 °C. (h) Durability test of the NiFeP/Ni₃S₂||Mo_{0.84}Ni_{0.16} AEM electrolyzer at 100 mA cm⁻² in 1.0 M KOH + seawater electrolyte.

the electrolyte was tested by starch potassium iodide paper and no ClO^- was found (Fig. S12), proving the unique OER selectivity of the as-prepared $\text{NiFeP}/\text{Ni}_3\text{S}_2$ amorphous/crystalline catalyst. It is also worth mentioning that the overall seawater splitting can be actuated by commercial solar panel under real sunlight. When the voltage of the solar panel is 2.03 V, the current density of overall seawater splitting can reach 120 mA cm^{-2} in 1.0 M KOH + seawater, and abundant gas bubbles can be clearly observed on the electrode surface (Fig. 6e), providing a feasible way for the realization of large-scale seawater electrolysis and renewable energy conversion. We further assembled an alkaline seawater anion exchange membrane (AEM) electrolyzer of $\text{NiFeP}/\text{Ni}_3\text{S}_2|\text{Mo}_{0.84}\text{Ni}_{0.16}$ to simulate the industrial-relevant environment (Fig. 6f). The AEM electrolyzer delivers current densities of 500 mA cm^{-2} at low cell voltages of 2.24 V and 2.51 V in 1.0 M KOH and 1.0 M KOH + seawater at ambient conditions, respectively (Fig. 6g). Meanwhile, the AEM electrolyzer was able to operate at 100 mA cm^{-2} for over 270 hours with negligible cell voltage perturbation (Fig. 6h), demonstrating the great potential of $\text{NiFeP}/\text{Ni}_3\text{S}_2$ for large scale application.

4. Conclusion

In summary, the $\text{NiFeP}/\text{Ni}_3\text{S}_2$ amorphous/crystalline heterogeneous electrode was successfully constructed for efficient and stable OER in alkaline seawater. Benefiting from the electronic structure optimization at the interfaces, the $\text{NiFeP}/\text{Ni}_3\text{S}_2$ shows overpotentials of 257 mV and 354 mV to drive current densities of 10 and 800 mA cm^{-2} in the alkaline medium, respectively. Moreover, only a cell voltage of 1.79 V is required to reach 100 mA cm^{-2} over 600 hours operation with two-electrode system ($\text{NiFeP}/\text{Ni}_3\text{S}_2|\text{Mo}_{0.84}\text{Ni}_{0.16}$) in alkaline seawater, and the assembled AEM electrolyzer has also been demonstrated to exhibit magnificent performance for commercial water electrolysis. Experimental profiles and DFT calculations have indicated that the constructed $\text{NiFeP}/\text{Ni}_3\text{S}_2$ heterointerface structure displays strong charge transfer ability and optimized adsorption for the OER intermediates. In situ Raman analysis and *operando* EIS analysis disclosed that the $\text{NiFeP}/\text{Ni}_3\text{S}_2$ amorphous/crystalline heterogeneous interface accelerated the reconstruction and the generation of active sites during OER process. We anticipate this design strategy will provide some inspirations for seawater electrolysis at commercial current density.

CCRediT authorship contribution statement

Lixue Zhang: Writing – review & editing, Validation, Supervision, Project administration, Funding acquisition, Formal analysis, Data curation, Conceptualization. **Yanyan Song:** Writing – review & editing, Writing – original draft, Validation, Methodology, Investigation, Formal analysis, Data curation, Conceptualization. **Zhengyi Xiao:** Data curation, Investigation. **Xiaoyan Zhang:** Supervision, Resources, Funding acquisition, Formal analysis, Data curation, Conceptualization, Validation, Writing – review & editing. **Peng Yi:** Methodology, Data curation. **Yue Wang:** Methodology. **Minghua Huang:** Validation, Supervision, Resources, Project administration, Funding acquisition, Formal analysis, Conceptualization.

Declaration of Competing Interest

The authors declare that they have no known competing financial interests or personal relationships that could have appeared to influence the work reported in this paper.

Data availability

Data will be made available on request.

Acknowledgements

This work was financially supported by the National Natural Science Foundation of China (Nos. 22075159, 22279124, and 22209088), Taishan Scholar Program (Nos. tsqn202103058, and tsqn202306173), the Fundamental Research Funds for the Central Universities (No. 202262010), the Free Exploration Project of Frontier Technology of Laoshan Laboratory (LSKJ202205400), and Qingdao New Energy Shandong Laboratory Open Project (QNESL OP202302).

Appendix A. Supporting information

Supplementary data associated with this article can be found in the online version at doi:10.1016/j.apcatb.2024.124028.

References

- [1] N.S. Lewis, Toward cost-effective solar energy use, *Science* 315 (2007) 798–801, <https://doi.org/10.1126/science.1137014>.
- [2] V.R. Stamenkovic, D. Strmcnik, P.P. Lopes, N.M. Markovic, Energy and fuels from electrochemical interfaces, *Nat. Mater.* 16 (2017) 57–69, <https://doi.org/10.1038/nmat4738>.
- [3] J.N. Tiwari, N.K. Dang, S. Sultan, P. Thangavel, H.Y. Jeong, K.S. Kim, Multi-heteroatom-doped carbon from waste-yeast biomass for sustained water splitting, *Nat. Sustain.* 3 (2020) 556–563, <https://doi.org/10.1038/s41893-020-0509-6>.
- [4] Z.W. Seh, J. Kibsgaard, C.F. Dickens, I.B. Chorkendorff, J.K. Norskov, T. F. Jaramillo, Combining theory and experiment in electrocatalysis: insights into materials design, *Science* 355 (2017) ead4998, <https://doi.org/10.1126/science.ead4998>.
- [5] J. Guo, Y. Zheng, Z. Hu, C. Zheng, J. Mao, K. Du, M. Jaroniec, S.-Z. Qiao, T. Ling, Direct seawater electrolysis by adjusting the local reaction environment of a catalyst, *Nat. Energy* 8 (2023) 264–272, <https://doi.org/10.1038/s41560-023-01195-x>.
- [6] Y. Song, T. Wang, J. Sun, Z. Wang, Y. Luo, L. Zhang, H. Ye, X. Sun, Enhanced electrochemical N_2 reduction to NH_3 on reduced graphene oxide by tannic acid modification, *ACS Sustain. Chem. Eng.* 7 (2019) 14368–14372, <https://doi.org/10.1021/acssuschemeng.9b03890>.
- [7] X.Y. Lu, C.A. Zhao, Electrodeposition of hierarchically structured three-dimensional nickel-iron electrodes for efficient oxygen evolution at high current densities, *Nat. Commun.* 6 (2015) 6616, <https://doi.org/10.1038/ncomms7616>.
- [8] Y. Song, M. Sun, S. Zhang, X. Zhang, P. Yi, J. Liu, B. Huang, M. Huang, L. Zhang, Alleviating the work function of vein-like Co_3P by Cr doping for enhanced seawater electrolysis, *Adv. Funct. Mater.* 33 (2023) 2214081, <https://doi.org/10.1002/adfm.202214081>.
- [9] W. Zang, T. Sun, T. Yang, S. Xi, M. Waqar, Z. Kou, Z. Lyu, Y.P. Feng, J. Wang, S. J. Pennycook, Efficient hydrogen evolution of oxidized Ni-N_3 defective sites for alkaline freshwater and seawater electrolysis, *Adv. Mater.* 33 (2021) 2003846, <https://doi.org/10.1002/adma.202003846>.
- [10] H. Xie, Z. Zhao, T. Liu, Y. Wu, C. Lan, W. Jiang, L. Zhu, Y. Wang, D. Yang, Z. Shao, A membrane-based seawater electrolyser for hydrogen generation, *Nature* 612 (2022) 673–678, <https://doi.org/10.1038/s41586-022-05379-5>.
- [11] H. Sun, J. Sun, Y. Song, Y. Zhang, Y. Qiu, M. Sun, X. Tian, C. Li, Z. Lv, L. Zhang, Nickel–cobalt hydrogen phosphate on nickel nitride supported on nickel foam for alkaline seawater electrolysis, *ACS Appl. Mater. Inter.* 14 (2022) 22061–22070, <https://doi.org/10.1021/acsaami.2c01643>.
- [12] L. Zhang, J. Liang, L. Yue, K. Dong, J. Li, D. Zhao, Z. Li, S. Sun, Y. Luo, Q. Liu, G. Cui, A. Ali Alshehri, X. Guo, X. Sun, Benzoate anions-intercalated NiFe -layered double hydroxide nanosheet array with enhanced stability for electrochemical seawater oxidation, *Nano Res.* 1 (2022) 9120028, <https://doi.org/10.26599/NRE.2022.9120028>.
- [13] X. Liu, Q. Yu, X. Qu, X. Wang, J. Chi, L. Wang, Manipulating electron redistribution in Ni_2P for enhanced alkaline seawater electrolysis, *Adv. Mater.* 13 (2023) 2307395, <https://doi.org/10.1002/adma.202307395>.
- [14] J. Cao, T. Mou, B. Mei, P. Yao, C. Han, X. Gong, P. Song, Z. Jiang, T. Frauenheim, J. Xiao, W. Xu, Improved electrocatalytic activity and stability by single iridium atoms on iron-based layered double hydroxides for oxygen evolution, *Angew. Chem. Int. Ed.* 62 (2023) e202310973, <https://doi.org/10.1002/anie.202310973>.
- [15] H. Jin, J. Xu, H. Liu, H. Shen, H. Yu, M. Jaroniec, S. Qiao, Emerging materials and technologies for electrocatalytic seawater splitting, *Sci. Adv.* 9 (2023) eadi7755, <https://doi.org/10.1126/sciadv.adi7755>.
- [16] S. Zhang, Y. Wang, S. Li, Z. Wang, H. Chen, L. Yi, X. Chen, Q. Yang, W. Xu, A. Wang, Z. Lu, Concerning the stability of seawater electrolysis: a corrosion mechanism study of halide on Ni-based anode, *Nat. Commun.* 14 (2023) 4822, <https://doi.org/10.1038/s41467-023-40563-9>.
- [17] Q. Wu, Q.P. Gao, B. Shan, W.Z. Wang, Y.P. Qi, X.S. Tai, X. Wang, D.D. Zheng, H. Yan, B.W. Ying, Y.S. Luo, S.J. Sun, Q. Liu, M. S. Hamdy, X.P. Sun, Recent advances in self-supported transition-metal-based electrocatalysts for seawater oxidation, *Acta Phys.-Chim. Sin.* 39 (2023) 2303012, <https://doi.org/10.3866/pku.Whxb202303012>.

- [18] J. Kang, X. Yang, Q. Hu, Z. Cai, L.-M. Liu, L. Guo, Recent progress of amorphous nanomaterials, *Chem. Rev.* 123 (2023) 8859–8941, <https://doi.org/10.1021/acs.chemrev.3c00229>.
- [19] C. Guo, Y. Shi, S. Lu, Y. Yu, B. Zhang, Amorphous nanomaterials in electrocatalytic water splitting, *Chin. J. Catal.* 42 (2021) 1287–1296, [https://www.cjcatal.com/EN/10.1016/S1872-2067\(20\)63740-8](https://www.cjcatal.com/EN/10.1016/S1872-2067(20)63740-8).
- [20] S. Shen, Z. Wang, Z. Lin, K. Song, Q. Zhang, F. Meng, L. Gu, W. Zhong, Crystalline-amorphous interfaces coupling of CoSe₂/CoP with optimized d-band center and boosted electrocatalytic hydrogen evolution, *Adv. Mater.* 34 (2022) 2110631, <https://doi.org/10.1002/adma.202110631>.
- [21] X. Zhang, Z.M. Luo, P. Yu, Y.Q. Cai, Y.H. Du, D.X. Wu, S. Gao, C.L. Tan, Z. Li, M. Q. Ren, T. Osipowicz, S.M. Chen, Z. Jiang, J. Li, Y. Huang, J. Yang, Y. Chen, C. Y. Ang, Y.L. Zhao, P. Wang, L. Song, X.J. Wu, Z. Liu, A. Borgna, H. Zhang, Lithiation-induced amorphization of Pd₃P₂S₈ for highly efficient hydrogen evolution, *Nat. Catal.* 1 (2018) 460–468, <https://doi.org/10.1038/s41929-018-0072-y>.
- [22] Y. Wang, X. Li, Z. Huang, H. Wang, Z. Chen, J. Zhang, X. Zheng, Y. Deng, W. Hu, Amorphous Mo-doped NiSe_{0.5}Se_{0.5} nanosheets@crystalline NiSe_{0.5}Se_{0.5} nanorods for high current-density electrocatalytic water splitting in neutral media, *Angew. Chem. Int. Ed.* 62 (2023) e202215256, <https://doi.org/10.1002/anie.202215256>.
- [23] T. Guo, L. Li, Z. Wang, Recent development and future perspectives of amorphous transition metal-based electrocatalysts for oxygen evolution reaction, *Adv. Energy Mater.* 12 (2022) 2200827, <https://doi.org/10.1002/aenm.202200827>.
- [24] L. Chai, S. Liu, S. Pei, C. Wang, Electrodeposited amorphous cobalt-nickel-phosphide-derived films as catalysts for electrochemical overall water splitting, *Chem. Eng. J.* 420 (2021) 129686, <https://doi.org/10.1016/j.cej.2021.129686>.
- [25] L. Song, Y. Qiu, X. Zhang, F. Liu, A. Li, Green strategy with high iron utilization for Cr (VI) removal via sodium polyacrylate-based hydrogel, *Chem. Eng. J.* 442 (2022) 136162, <https://doi.org/10.1016/j.cej.2022.136162>.
- [26] S. Zhao, Y. He, Z. Wang, X. Bo, S. Hao, Y. Yuan, H. Jin, S. Wang, Z. Lin, Advancing performance and unfolding mechanism of lithium and sodium storage in SnO₂ via precision synthesis of monodisperse PEG-ligated nanoparticles, *Adv. Energy Mater.* 12 (2022) 2201015, <https://doi.org/10.1002/aenm.202201015>.
- [27] P. Yi, Y.Y. Song, C.Y. Li, R.Z. Liu, J.K. Sun, Heterostructured Mn-doped NiSe₂/NiO/Ni₃N nanoplate arrays as bifunctional electrocatalysts for energy-saving hydrogen production and urea degradation, *Appl. Surf. Sci.* 619 (2023) 156789, <https://doi.org/10.1016/j.apsusc.2023.156789>.
- [28] H. Zhang, J. Diao, M. Ouyang, H. Yadegari, M. Mao, M. Wang, G. Henkelman, F. Xie, D.J. Riley, Heterostructured core-shell Ni-Co@Fe-Co nanoboxes of prussian blue analogues for efficient electrocatalytic hydrogen evolution from alkaline seawater, *ACS Catal.* 13 (2023) 1349–1358, <https://doi.org/10.1021/acscatal.2c05433>.
- [29] K. Wang, J. Wu, S. Zheng, S. Yin, NiCo alloy nanoparticles anchored on mesoporous Mo₂N nanosheets as efficient catalysts for 5-hydroxymethylfurfural electrooxidation and hydrogen generation, *Chin. J. Struct. Chem.* 42 (2023) 100104, <https://doi.org/10.1016/j.cjcs.2023.100104>.
- [30] L. Hou, H. Jang, X. Gu, X. Cui, J. Tang, J. Cho, X. Liu, Design strategies of ruthenium-based materials toward alkaline hydrogen evolution reaction, *EcoEnergy* 1 (2023) 16–44, <https://doi.org/10.1002/ece2.4>.
- [31] S. Zhao, Y. Wang, Y. Hao, L. Yin, C.-H. Kuo, H.-Y. Chen, L. Li, S. Peng, Lewis acid driving asymmetric interfacial electron distribution to stabilize active species for efficient neutral water oxidation, *Adv. Mater.* 36 (2023) e2308925, <https://doi.org/10.1002/adma.202308925>.
- [32] X. Luo, P. Ji, P. Wang, X. Tan, L. Chen, S. Mu, Spherical Ni₃S₂/Fe-NiP_x Magic cube with ultrahigh water/seawater oxidation efficiency, *Adv. Sci.* 9 (2022) 2104846, <https://doi.org/10.1002/advs.202104846>.
- [33] Z. Wang, W. Xu, X. Chen, Y. Peng, Y. Song, C. Lv, H. Liu, J. Sun, D. Yuan, X. Li, X. Guo, D. Yang, L. Zhang, Defect-rich nitrogen doped Co₃O₄/C porous nanocubes enable high-efficiency bifunctional oxygen electrocatalysis, *Adv. Funct. Mater.* 29 (2019) 1902875, <https://doi.org/10.1002/adfm.201902875>.
- [34] S. Zhang, Y. Wang, X. Wei, L. Chu, W. Tian, H. Wang, M. Huang, Dual interface-reinforced built-in electric field for chlorine-free seawater oxidation, *Appl. Catal. B* 336 (2023) 122926, <https://doi.org/10.1016/j.apcatb.2023.122926>.
- [35] S. Zhang, C. Tan, R. Yan, X. Zou, F.L. Hu, Y. Mi, C. Yan, S. Zhao, Constructing built-in electric field in heterogeneous nanowire arrays for efficient overall water electrolysis, *Angew. Chem. Int. Ed.* 135 (2023) e202302795, <https://doi.org/10.1002/anie.202302795>.
- [36] Y. Zeng, M. Zhao, Z. Huang, W. Zhu, J. Zheng, Q. Jiang, Z. Wang, H. Liang, Surface reconstruction of water splitting electrocatalysts, *Adv. Energy Mater.* 12 (2022) 2201713, <https://doi.org/10.1002/aenm.202201713>.
- [37] Q. Cai, W. Hong, C. Jian, X. He, W. Liu, Recent development of self-supported alkaline hydrogen evolution reaction electrocatalysts for industrial electrolyzer, *Adv. Energy Sustain. Res.* 4 (2023) 2200178, <https://doi.org/10.1002/aesr.202200178>.
- [38] P. Zhai, C. Wang, Y. Zhao, Y. Zhang, J. Gao, L. Sun, J. Hou, Regulating electronic states of nitride/hydroxide to accelerate kinetics for oxygen evolution at large current density, *Nat. Commun.* 14 (2023) 1873, <https://doi.org/10.1038/s41467-023-37091-x>.
- [39] W. Tong, M. Forster, F. Dionigi, S. Dresp, R. Sadeghi Erami, P. Strasser, A.J. Cowan, P. Farràs, Electrolysis of low-grade and saline surface water, *Nat. Energy* 5 (2020) 367–377, <https://doi.org/10.1038/s41560-020-0550-8>.
- [40] L. Wu, L. Yu, B. McElhenny, X. Xing, D. Luo, F. Zhang, J. Bao, S. Chen, Z. Ren, Rational design of core-shell-structured CoP₂@FeOOH for efficient seawater electrolysis, *Appl. Catal. B* 294 (2021) 120256, <https://doi.org/10.1016/j.apcatb.2021.120256>.
- [41] J. Li, Y. Liu, H. Chen, Z. Zhang, X. Zou, Design of a multilayered oxygen-evolution electrode with high catalytic activity and corrosion resistance for saline water splitting, *Adv. Funct. Mater.* 31 (2021) 2101820, <https://doi.org/10.1002/adfm.202101820>.
- [42] Z. Li, Y. Yao, S. Sun, J. Liang, S. Hong, H. Zhang, C. Yang, X. Zhang, Z. Cai, J. Li, Y. Ren, Y. Luo, D. Zheng, X. He, Q. Liu, Y. Wang, F. Gong, X. Sun, B. Tang, Carbon oxanion self-transformation on NiFe oxalates enables long-term ampere-level current density seawater oxidation, *Angew. Chem. Int. Ed.* 63 (2024) e202316522, <https://doi.org/10.1002/anie.202316522>.
- [43] W. Xu, Z. Wang, P. Liu, X. Tang, S. Zhang, H. Chen, Q. Yang, X. Chen, Z. Tian, S. Dai, L. Chen, Z. Lu, Ag nanoparticle-induced surface chloride immobilization strategy enables stable seawater electrolysis, *Adv. Mater.* 36 (2024) 2306062, <https://doi.org/10.1002/adma.202306062>.
- [44] L. Li, G. Zhang, J. Xu, H. He, B. Wang, Z. Yang, S. Yang, Optimizing the electronic structure of ruthenium oxide by neodymium doping for enhanced acidic oxygen evolution catalysis, *Adv. Funct. Mater.* 33 (2023) 2213304, <https://doi.org/10.1002/adfm.202213304>.
- [45] W.W. Xu, Z.Y. Lu, X.M. Sun, L. Jiang, X. Duan, Superwetting electrodes for gas-involving electrocatalysis, *Acc. Chem. Res.* 51 (2018) 1590–1598, <https://doi.org/10.1021/acs.accounts.8b00070>.
- [46] S. Zhang, W. Wang, F. Hu, Y. Mi, S. Wang, Y. Liu, X. Ai, J. Fang, H. Li, T. Zhai, 2D CoOOH sheet-encapsulated Ni₂P into tubular arrays realizing 1000 mA cm⁻²-level-current-density hydrogen evolution over 100h in neutral water, *Nano-Micro Lett.* 12 (1) (2020) 16, <https://doi.org/10.1007/s40820-020-00476-4>.
- [47] J. Zhu, J. Chi, T. Cui, L. Guo, S. Wu, B. Li, J. Lai, L. Wang, F doping and P vacancy engineered FeCoP nanosheets for efficient and stable seawater electrolysis at large current density, *Appl. Catal. B* 328 (2023) 122487, <https://doi.org/10.1016/j.apcatb.2023.122487>.
- [48] D. Chen, R. Lu, R. Yu, Y. Dai, H. Zhao, D. Wu, P. Wang, J. Zhu, Z. Pu, L. Chen, Work-function-induced interfacial built-in electric fields in Os-OsSe₂ heterostructures for active acidic and alkaline hydrogen evolution, *Angew. Chem. Int. Ed.* 61 (2022) e202208642, <https://doi.org/10.1002/anie.202208642>.
- [49] J. Liu, J. Huang, J. Sun, Y. Song, J. Yang, Q. Chen, X. Zhang, L. Zhang, Rapid synthesis of NiMo-based electrocatalysts at room temperature for efficient oxygen and hydrogen evolution in seawater, *J. Electroanal. Chem.* 935 (2023) 117311, <https://doi.org/10.1016/j.jelechem.2023.117311>.